Influence of the electrode/electrolyte interface structure on the performance of Pr0.8Sr0.2Fe0.7Ni0.3O3-δ as Solid Oxide Fuel Cell cathode

Alice Giuliano, Clement Nicollet, Sébastien Fourcade, Fabrice Mauvy, Maria Paola Carpanese, Jean-Claude Grenier

Influence of the electrode/electrolyte interface structure on the performance of $Pr_{0.8}Sr_{0.2}Fe_{0.7}Ni_{0.3}O_{3-\delta}$ as Solid Oxide Fuel Cell cathode

Giuliano A.[a,b], Nicollet C.[b], Fourcade S.[b], Mauvy F.[b], Carpanese M. P.[a,c], Grenier J.-C.[b]

a Department of Civil, Chemical and Environmental Engineering (DICCA), University of Genoa P.le J.F. Kennedy 1, I-16129 Genova, Italy
[b] CNRS, Université de Bordeaux, ICMCB, 87 Avenue du Dr. Schweitzer, F-33608 Pessac Cedex, France
[c] Institute of Condensed Matter Chemistry and Technology for Energy (CNR-ICMATE), Via De Marini 6, I-16149 Genova, Italy

Corresponding author at: Department of Civil, Chemical and Environmental Engineering (DICCA), University of Genoa P.le J.F. Kennedy 1, I-16129 Genova, Italy.

Abstract :

The effect of gadolinium-doped ceria (GDC) interlayer on the $Pr_{0.8}Sr_{0.2}Fe_{0.7}Ni_{0.3}O_{3-\delta}$ (PSFN8273) cathode performance and stability in solid oxide fuel cell (SOFC) operating conditions is investigated. Two different symmetrical half-cells, with dense GDC electrolyte pellet (GDC/PSFN cell) and with GDC interlayer deposited on yttria stabilized zirconia pellet (YSZ) (YSZ/GDC/PSFN cell), are prepared and characterized by electrochemical impedance spectroscopy (EIS) as a function of temperature. The fitting of the data is carried out using an adapted Equivalent Circuit (EC). The polarization resistance (R_p) is higher for the YSZ/GDC/PSFN cell compared to GDC/PSFN cell. This increase is assigned to the interface microstructure. Then, the electrochemical properties of the half-cell with GDC interlayer are measured in three-electrode configuration under dc cathodic overpotential. In addition, the long-term stability is evaluated through an ageing test applying a current density of −123 mA.cm^{-2} for 1000 hours at 700 °C under air. PSFN8273 appears to be stable as cathode with a decrease in overpotential of about 6% in the first 200 hours and a subsequently stabilization. These results mean that even if the GDC interlayer affect the cathode performance (in terms of R_p) it did not influence its stability, making PSFN8273 a suitable material as cathode for SOFC application.

1. Introduction

Solid oxide fuel cells (SOFCs) are highly efficient energy conversion devices able to convert chemical energy in electrical energy. As they operate at high temperature (800–1000 °C), their lifetime is limited by thermal degradation via coarsening of particles in the electrodes and chemical reactivity between the electrolyte and the electrodes. Typical materials are, for the electrolyte, the yttria doped (8%) zirconia (so called 8YSZ), for the anode, a Ni-8YSZ cermet, for the cathode, the lanthanum strontium manganite $La_{1-x}Sr_xMnO_3$ (LSM) or a composite of LSM/YSZ [1]; [2]; [3] ; [4].

Many efforts have been focused on developing new electrode materials as well as minimizing the polarization resistance of these conventional electrode materials by optimizing their microstructures and compositions, so that they can be operated at intermediate temperatures (500 − 700 °C). In recent years, mixed ionic and electronic conductor (MIEC) perovskite materials, like $La_{0.6}Sr_{0.4}Fe_{0.8}Co_{0.2}O_{3-\delta}$ (LSCF), have been intensively investigated as cathode for intermediate temperature solid oxide fuel cells (IT-SOFCs) [5]. However, LSCF has relatively high thermal expansion coefficient (TEC) compared to that of usual electrolytes like yttria stabilized zirconia (YSZ) [6] or CeO_2 based ones [7]. This difference in TEC can induce thermal stresses at the electrolyte/electrode interface in operating conditions, leading to cracking or delamination.

Replacing La by Pr in $La_{1-x}Sr_xMnO_{3\pm\delta}$ (LSM) or $La_{1-x}Sr_xCoO_{3-\delta}$ (LSC) well-known cathode materials is useful to improve their electrical conductivity [8]; [9] ; [10]. Moreover their impregnation in LSCF cathode backbone enhances the cathode performance [11]. In the literature, other candidates are Fe-Ni based perovskites, in particular $La_{1-y}Sr_yNi_{1-x}Fe_xO_3$ system that shows high electrical conductivity (500 − 700 S cm^{-1} at 600 °C) [12] and good electrocatalytic properties [13].

Thus, a combination of Pr and Sr for A-site and Fe and Ni for B-site in the ABO_3 perovskite structure was reported by some authors to exhibit better electrochemical properties as cathode material at low temperature. Hashimoto et al. [14] found relatively good results in the study of $Pr_{0.7}Sr_{0.3}Fe_{0.7}Ni_{0.3}O_{3-\delta}$ with an electrical conductivity of 400 S cm^{-1} at 600 °C and a polarization resistance (R_p) of 0.30 Ω cm^2 at 800 °C. Pinedo et al. [15] studied different synthesis routes for $Pr_{0.7}Sr_{0.3}Fe_{0.8}Ni_{0.2}O_3$, obtaining a R_p value of 0.56 Ω cm^2 at 850 °C.

Another important aspect to take in account in these systems is the long-term stability. Many studies were devoted, in the recent years, to develop materials, microstructures and specific cell assemblies, especially to overcome the cathode degradation, considered as one of the main cause of SOFCs performance decrease. In particular, the cobalt- and ferrite-based perovskites have the drawback of forming insulating phases with pyrochlore-type materials, such as $La_2Zr_2O_7$ (LZO) and $Pr_2Zr_2O_7$ (PZO), and with perovskite structure such as $SrZrO_3$ (SZO), at the interface between the electrode and the YSZ electrolyte [16]. Such materials have very poor oxygen ionic conductivity even at high temperature, which results in a high additional ohmic resistance [17]. To prevent the zirconate formation, Gd-doped ceria (GDC) has been considered as an alternative electrolyte for low temperature SOFCs, and is also one of the most efficient interlayers set between the cathode and YSZ electrolyte. As barrier layer, the GDC layer should be as thin and dense as possible [18]. However, GDC has poor sintering properties and (Zr, Ce)O_2-based solid solutions can be formed when the GDC interlayer is sintered on the YSZ electrolyte [19], which can limit the interfacial oxide ion diffusion. Efforts have been made by many researchers to optimize this interlayer in order to obtain a better electrochemical performance. Song et al. [20] and Flura et al. [21] determined that the cathode performance is strongly dependent on the microstructure of the layer and, as a consequence, on the fabrication conditions, as sintering temperature, sintering aid addition, particle size. Khan et al. [22] recently published an article about the influence of GDC interlayer thickness, Szasz et al. [23] analysed the formation of SZO with different porosity of GDC and finally Wang et al. [24] tried to densify the GDC interlayer starting from a pulsed laser deposition (PLD), which minimizes the Sr and Zr diffusion but does not avoid it.

In the present paper, a new composition of the PSFN system, containing less Sr content, $Pr_{0.8}Sr_{0.2}Fe_{0.7}Ni_{0.3}O_{3-\delta}$ (PSFN8273), is synthesized and characterized as cathode in half-cell configuration. Cathodes are deposited either on a dense GDC electrolyte or on a dense YSZ with a GDC interlayer and the results are compared in order to evaluate the effect of GDC interlayer on the PSFN8273 performance. An ageing test at 700 °C under current load is performed on the half-cell with the GDC interlayer for 1000 hours under air, with regard to the possible changes in cathode catalytic activity and the aforementioned secondary phase formation at the interface.

The cell performance is characterized by Electrochemical Impedance Spectroscopy (EIS), which allows discriminating the interface transport process and the oxygen reduction reaction (ORR) contributions.

2. Experimental

2.1. Powder preparation

The PSFN8273 phase was synthesized using the Glycine Nitrate Process (GNP) [25], starting from 1 M solution of $Pr(NO_3)_3{\cdot}6H_2O$ (Sigma Aldrich), $Sr(NO_3)_2$ (Alfa Aesar), $Fe(NO_3)_3{\cdot}9H_2O$ (Sigma Aldrich), and $Ni(NO_3)_3{\cdot}6H_2O$ (Alfa Aesar) precursors and glycine. The solution was heated and stirred on a hot plate at 200 °C for 2 hours to evaporate water, and then placed on a Bunsen burner to complete the reaction and to obtain nano-powders.

The obtained powder was then annealed at 1000 °C for 2 hours under air to crystallize the phase and ground in a mortar for 1 hour.

2.2. Structural and microstructural investigation

The PSFN powder and the electrode/electrolyte interface were characterized by X-Ray diffraction (XRD) using a PANanalytical X'pert MPD diffractometer with Cu-K_α incident radiation. Diffractograms were recorded over the angular range 20° < 2 θ < 80 °, in a constant scan mode with steps of 0.02 ° and a counting time of 40 s.

The microstructure of PSFN8273 powder and the electrode morphology were observed by Scanning Electron Microscopy (JEOL JSM 6330F) equipped with an EDS detector. The thickness of the electrode and the electrolytes were measured and their porosity determined by means of image thresholding analysis using the Image J software and compared with geometrical apparent density measurements.

2.3. Preparation of symmetrical half cells

Three different electrolyte substrates were made for the symmetrical half − cell assembly.

i) PSFN//YSZ//PSFN (namely YSZ/PSFN cell): dense pellets of 8YSZ (8 mol% yttria stabilized zirconia −Tosoh) with diameter ∼ 18 mm and thickness ∼ 1.6 mm were sintered at T = 1400 °C for 12 hours.

ii) PSFN//GDC//PSFN (namely GDC/PSFN cell): $Ce_{0.8}Gd_{0.2}O_{1.90}$ (GDC20, Marion Technology) powders were pressed into pellets, after a step of mixing in a mortar with Polyvinyl alcohol (PVA). The pellets were sintered at 1400 °C for 12 hours, achieving a density of 94% with ∼19 mm diameter and ∼ 1.5 mm thickness.

iii) PSFN//GDC//8YSZ//GDC//PSFN (namely YSZ/GDC/PSFN cell): dense pellets of 8YSZ as point (i) were pressed and sintered. Then, following previous studies [21]; [23] ; [28], 2–3 µm GDC layers were screen printed on both sides of these electrolyte pellets and sintered at 1350 °C for 3 hours [21].

Finally, PSFN8273 electrodes were symmetrically deposited as working (WE) and counter (CE) electrodes on both sides of the electrolyte pellets by screen printing and sintered at 1100 °C for 2 hours, with an intermediate step at 400 °C to burn the organics from the slurry.

2.4. Electrochemical measurements

Electrochemical impedance spectroscopy (EIS) measurements were performed using an home-made setup [21], on the symmetrical half-cells in two and three-electrode configuration, placing a platinum ring around the circumference of the electrolyte pellet as reference electrode [26] ; [27]. Impedance measurements were carried out in the range 10^5 Hz – 10^{-1} Hz, at open circuit voltage (OCV), and different cathodic dc voltages, using a Modulab XM series (Ametek) potentiostat and frequency response analyser, with applied amplitude of 50 mV. Gold grids were used as current collectors. The temperature dependent measurements were conducted in the temperature range of 550 − 800 °C, in air. At each temperature, a stabilization period of 20 min was achieved before the acquisition.

An ageing test of 1000 hours under direct current application was performed on the YSZ/GDC/PSFN cell to simulate the SOFC operating conditions (T = 700 °C).

The obtained impedance diagrams were fitted using the ZView software (Scribner Associates Inc.); the equivalent circuit (EC) selected for the fits consisted in a combination of R//CPE elements connected in series with the electrolyte resistance (R_s).

3. Results and discussion

3.1. Structural and morphology characterizations

Fig. 1a shows the XRD pattern of the calcined PSFN8273 powders at room temperature. The material crystallized in a single-phase orthorhombic $PrFeO_3$-type structure (*Pbnm* space group), which is a distorted perovskite, and similar to those of $Pr_{0.7}Sr_{0.3}Fe_{0.7}Ni_{0.3}O_{3-\delta}$[14] and $La_{1-y}Sr_yFe_{1-x}Ni_xO_{3-\delta}$[12]. The SEM micrograph (Fig. 1b) of the annealed powder shows aggregated homogeneous particles of about 50 nm in diameter; after a step in a three-roll miller, a slurry of this powder was then applied directly on the electrolyte substrates by screen printing [21]. Fig. 2a shows a GDC/PSFN cell fractured cross section after the sintering cycle, the electrode thickness is around 20 µm and homogeneous over the whole sample, the electrode porosity, estimated using ImageJ software, is around 40%. On the other hand, an enlargement at the electrode/electrolyte interface of the YSZ/GDC/PSFN cell fractured cross section is given in Fig. 2b, showing distinctly the three layers (YSZ electrolyte, GDC porous interlayer, PSFN electrode). The GDC interlayer is around 2 µm thick and homogeneously applied on the YSZ dense electrolyte, with a density of about 80% evaluated by ImageJ analyser.

3.2. Influence of the electrolyte/electrode interface

To study the influence of the electrolyte/electrode interface on the electrochemical performance, EIS at i_{dc} = 0 were performed on the three cells (YSZ/PSFN, GDC/PSFN, and YSZ/GDC/PSFN). In Fig. 3a, the Nyquist plots of YSZ/PSFN cell at 700 °C and 800 °C show high polarization resistances (R_p = 162 Ω cm^2 at 700 °C and 27.7 Ω cm^2 at 800 °C), determined as the difference between the low and high frequency intercepts of the impedance diagrams with the real axis. As mentioned in the introduction, the high R_p in the YSZ-supported systems could be ascribed to the formation of secondary less-conductive phases, like $SrZrO_3$ and $Pr_2Zr_2O_7$. In order to evaluate the presence of these phases, the PSFN electrode was mechanically removed after the electrochemical test, and the interface was analysed by XRD; the results are reported in Fig. 3b. The pattern clearly shows the YSZ peaks and the occurrence of the $SrZrO_3$ phase, which could be effectively responsible of the high polarization resistance; the Strontium Zirconate cubic phase presence is also confirmed by Fig. 3b inset, where the intensity logarithm vs. 2 theta is reported, in order to better individuate its peaks.

With the aim to avoid this behaviour, two other electrolyte substrate were prepared as presented in the preparation of symmetrical cells (paragraph 2.3). The electrochemical properties of the obtained GDC/PSFN and YSZ/GDC/PSFN cells were then characterized. In Fig. 4a, the Nyquist plots of GDC/PSFN and YSZ/GDC/PSFN cells, at 700 °C, exhibit a completely different behaviour. Firstly, the R_p increases from 0.71 Ω cm^2 (GDC/PSFN cell), which is in the same order of magnitude of the most used MIEC cathode materials [16], up to 1.95 Ω cm^2 (YSZ/GDC/PSFN cell). Secondly, the shape of both plots is different, showing for the YSZ/GDC/PSFN cell two well separated time constants, confirmed by the Bode plot (Fig. 4b). The peak attributed to the cathode behaviour (low frequencies) changes from 251 Hz for GDC/PSFN cell to 199 Hz for YSZ/GDC/PSFN cell, due to the influence of the high frequency peak (3981 Hz), ascribed to the electrode/electrolyte interface in YSZ/GDC/PSFN, that becomes weaker for the GDC/PSFN cell (see discussion below). In Table 1, the values of R_p obtained with PSFN 8273 in these two half-cell configurations are, compared with results reported in literature for other PSFN compositions. The impedance spectra, from 600 °C to 800 °C, were fitted with an appropriate equivalent circuit (Fig. 5a) to evaluate the effect of temperature on the electrochemical properties. The red lines overlapped to the impedance diagrams in Fig. 4 a represent the fits obtained with an equivalent circuit composed of two R//CPE elements connected in series with the electrolyte resistance (*Rs*) and an inductance (*L*), discriminating the two contributions at high frequencies (HF) and low frequencies (LF) (Fig. 5a). Based on previous works [29], the HF arc is assigned to the ionic oxide transfer at the interface electrode/electrolyte since the LF arc reflects the oxygen reduction reaction (ORR).

Starting from the CPE values obtained from ZView software, the equivalent capacitance (C_{eq}) was calculated using the equation:

$$C_{eq} = R^{\frac{1-n}{n}} \cdot Q^{\frac{1}{n}} \quad (1)$$

Where R is the resistance of the R//CPE element, Q is the module of the capacitance value given by the software and n is an exponential parameter [30]. Fig. 5b shows the resistance of the HF circuit (R_{HF}) and the one of the LF circuit (R_{LF}) as a function of temperature for GDC/PSFN and YSZ/GDC/PSFN cells. The R_{LF} thermal variation is quite similar between both cells with different electrolyte substrates, indicating that the process kinetics for the two electrodes is the same. On the other hand, the R_{HF} one significantly differs. R_{HF} – YSZ/GDC/PSFN cell is higher than R_{HF} – GDC/PSFN cell throughout the whole temperature range, suggesting a reduced ionic transfer kinetics from the electrode to the GDC porous interlayer. It could be due to the lower contact area compared to a dense GDC or to some reactivity between YSZ/GDC/PSFN with formation of additional phases during the sintering process as pointed out by Flura et al. [21]. All the activation energies of R_{HF} and R_{LF} are around 1.50-1.60 eV. From an electrochemical point of view, as claimed by Maier et al. [31] and Fleig et al. [32], the change of the oxygen content in the electrode bulk results in a capacitive process; in the literature, it has been referred to as "chemical" capacitance (C_{chem}) [31] with values in a range from 10^{-3} to 10 F.cm^{-2}[33], and should reflect the bulk defect chemical change inside the electrode material [32]. In our results, C_{LF} is associated to this C_{chem} (Fig. 5c). The C_{chem} value that is 3.38 × 10^{-3} F.cm^{-2} for the GDC/PSFN cell at 600 °C, increases up to 3.56 × 10^{-3} F.cm^{-2} at 800 °C, which could be related to the increase of oxygen vacancies concentration [33]. Other capacitances that are frequently observed in solid state electrochemistry such as electrostatic double layer or grain boundary capacitances are order of magnitude smaller [34] ; [35]. Thus, the value of C_{LF} is consistent with a chemical capacitance. The increase of C_{LF} was also observed in the case of YSZ/GDC/PSFN cell (from 4.54 × 10^{-4} F.cm^{-2} at 600 °C to 1.71 × 10^{-3} F.cm^{-2} at 800 °C) but the lower values suggest an influence of the interface area.

The values of capacitance associated with the high frequency semicircle (C_{HF}) are 33 µF cm^{-2} at 600 °C and 52 µF cm^{-2} at 800 °C for the YSZ/GDC/PSFN cell. In the experiments with the GDC/PSFN cell, from the peak frequencies of Fig. 4b, the value of C_{HF} reaches 256 µF cm^{-2} at 800 °C; such an increase is likely due to the different interactions at electrode/electrolyte interface between the two supported half-cells. Thus, the increase of C_{HF} with the increase of temperature could be interpreted as a charge accumulation at interface electrode/electrolyte.

Finally, according to the associated capacitive effects reported in Fig. 5c and by comparison with literature data [31] ; [36], it is confirmed that the R_{HF}//CPE_{HF} circuit is associated to the oxygen ionic ($O^{=}$) transfer from the electrocatalyst (PSFN) to the electrolyte at the cathode/electrolyte interface and the R_{LF}//CPE_{LF} arc is assigned to the Oxygen Reduction Reaction (ORR). R_{LF} gives information about the kinetics of this process, while CPE_{LF} is associated to the charge stored in the oxygen vacancies in the electrocatalyst volume.

3.3. YSZ/GDC/PSFN behaviour under dc current

As demonstrated in the previous paragraph, the high frequency contribution is larger for the YSZ/GDC/PSFN, suggesting that the increase in the global R_p can be mainly attributed to the interface microstructure and probably to reactivity/interdiffusion problems. To better understand the influence of the electrolyte/electrode interface on the PSFN8273 performance, the working electrode of YSZ/GDC/PSFN cell was polarized applying a dc overpotential (E_{dc}), in the range 0 to −1 V. Under cathodic potential ($\eta_{cathode}$) there is a net flux of oxygen species from the gas phase through the WE into the electrolyte, followed by the release to the gas phase at the CE.

The resulting cathodic overpotential can be calculated under steady state conditions from the following equation:

$$\eta_{cathode} = E_{dc} - j_{dc}R_s \quad (2)$$

where E_{dc} is the applied dc bias, j_{dc} is the direct current density and R_s is the electrolyte resistance.

Fig. 6a shows a typical example of the cathodic polarization curve for PSFN8273 electrode measured at 700 °C. Starting from the Butler-Volmer equation, in low overpotential regime, the relation of overpotential $\eta_{cathode}$ *vs.* current density can be expressed by the following linear equation [37]:

$$\eta_{cathode} = \frac{RT}{nFj_0} j_{dc} \quad (3)$$

where j_0 is the exchange current density, n is the number of electrons involved in the electrode reaction, F is the Faraday constant, R is the gas constant, and T is the measured temperature. The term RT/nFj_0 is directly related to the polarization resistance under zero dc condition (Eq. (4)).

$$R_p = \frac{RT}{nFj_0} \quad (4)$$

The exchange current density j_0 value corresponds to the x-intercept of the $\eta_{cathode}$ *vs*. *log* j_{dc} plot and is calculated using the Tafel relation (Eq. (5)) [38]:

$$logj_{dc} = logj_0 + \frac{\alpha nF}{2.3 \times RT} \times \eta_{cathode} \quad (5)$$

where α is the charge transfer usually assumed to be 0.5.

The j_0 obtained value is around 50 mA cm^{-2}; from this value, the R_p was calculated from Eq. (4) and compared with the experimental data at 700 °C, at the zero dc condition. Taking into account the experimental errors, the two values are in good agreement, R_p = 1.68 Ω cm^2 from Eq. (4) (Tafel relation) calculation and R_p = 1.95 Ω cm^2 from Nyquist plot (Fig. 5b), confirming the stability of the electrode under j_{dc}. In addition, this current exchange density is in the same order of those reported in literature for $Pr_{0.8}Sr_{0.2}FeO_3$ (34.3 mA.cm^{-2} at 750 °C) [39] and for $La_{0.6}Sr_{0.4}Co_{0.2}Fe_{0.8}O_{3-\delta}$ cathodes (65 mA.cm^{-2} at 700 °C) [40], lower than that of $Ba_{0.5}Sr_{0.5}Co_{0.8}Fe_{0.2}O_{3-\delta}$ cathode (182 mA.cm^{-2} at 700 °C) [41], and much larger than those of the ionic conductor $Pr_{0.55}Sr_{0.4}MnO_3$ cathode (2.80 mA.cm^{-2} at 750 °C) [42]. Fig. 6b shows the impedance diagrams at 700 °C in air for different dc bias. The Nyquist plots were fitted with the equivalent circuit shown in Fig. 5a to determine the total polarization resistance and the resistances as well as the equivalent capacitances of the two circuits. The total R_p decreases with the increase of the cathodic overpotential (Fig. 6b), as well as R_{HF} and R_{LF} (Fig. 6c). The decrease of the two values are of the same order of magnitude, suggesting that the ionic transfer mechanism at the electrolyte/electrode interface and in the bulk of the electrode is accelerated by the application of a bias with an increase in oxygen surface activity, probably due to the high concentration of oxygen vacancies for O^{2-} accommodation [43]. Regarding the C_{eq} (expressed in Eq. (1)) (Fig. 6d), C_{HF} remains almost stable, suggesting that there is no accumulation of charges at the interface. On the other hand, the chemical capacitance (C_{LF}) increases, reaching C_{LF} = 0.019 F cm^{-2} (at $\eta_{cathode}$ = − 0.26 V/Pt/Air). As previously mentioned, C_{chem} is connected to the bulk defect chemical

changes, and, due to cathodic overpotential, a change in electron concentration (*i.e.* a decrease of the valence of the 3d cations) takes place [44], which enhances the formation of oxygen vacancies reflected in an increase of C_{LF}. As mentioned in the introduction, one of the most important issues for a material used as cathode in solid oxide fuel cells is the stability under operating conditions. It is possible to simulate the working condition by the application of a current load over time to the cathode. The reaction that occurs to the WE is the oxygen reduction reaction (ORR) (Eq. (6)).

$$\frac{1}{2}O_2 + 2e^- \rightarrow O^{2-} \qquad (6)$$

The experimental value of current load was selected from the graph in Fig. 5a; to ensure an overpotential between −0.4 and −0.35 V/Pt/Air, a current load of −123 mA cm^{-2} was applied to the cathode (WE) over time. During the test, the current was periodically interrupted for the time necessary to perform the EIS measurements at OCV and to follow up the change in the cathode activity. Fig. 7a shows the variation of the cathode overpotential module ($|\eta_{cathode}|$) as a function of time. In the first 200 hours a decrease of $\eta_{cathode}$ is observed with a subsequent stabilization up to 1000 hours, the calculated $\Delta\eta$ over the 200 hours is about 6%. This decrease in cathodic overpotential is reflected in the total R_p decrease (*cf.* impedance diagrams Fig. 7b). In Bode plots (not presented here), the two time constants, at high and low frequencies, as observed in Fig. 4b, are still present. The HF peak defined by the frequency maximum (f_{max}) and attributed to the O^{2-} transfer at the interface electrode/electrolyte, decreases from 3981 Hz to 1584 Hz. In previous works [45]; [46] ; [47], a similar cathode behaviour was associated to microstructural and morphological changes under a current flow, due to a beneficial electrode porosity refining.

The interpretation of the parameters of the equivalent circuit, presented in the previous section, might be useful to better understand the oxygen process at the electrode. In Fig. 7c, R_{HF} and R_{LF} variations are reported: an initial decrease of about 6 % in 200 hours is observed. The possibility of a porosity refinement of the electrode surface/bulk and at interface could be an acceptable explanation. After this stabilization period, the impedance diagrams are overlapped and the values of R_{HF} and R_{LF} are constant until 1000 hours, suggesting a high electrode stability compared to other cathode materials as reported in the literature as the state of the art [48]; [49] ; [50] and also to very recent materials [51]. Observing the equivalent capacitance trends, a slow change in bulk defect chemistry, may be due to the current load application, could explain the C_{chem} (C_{LF}) increase. Finally, Fig. 8a and b show the YSZ/GDC/PSFN cell fractured cross section SEM images before and after the electrochemical test, respectively. No significant microstructural changes can be detected. It is likely that the GDC microstructure (either densification or Pr diffusion [52]) affects the impedance results reflected in the decrease of R_{HF} in the first 200 hours (Fig. 7c).

On the other hand, the total R_p increase of YSZ/GDC/PSFN cell compared to the GDC/PSFN cell can be attributed to the formation of PZO second phase; actually, from the XRD pattern obtained at the YSZ/GDC/PSFN interface after removing the electrode, $Pr_2Zr_2O_7$ peaks are detected (Fig. 8c). This pattern corresponds to the cell investigation after the sintering process and is the same after polarization for 1000 hours, suggesting that the PZO phase is formed during the thermal treatment and is maintained during the ageing test without any other structural modifications.

4. Conclusions

A new stoichiometry of the PSFN perovskite material was synthesized and deeply studied as cathode for solid oxide fuel cells by electrochemical impedance spectroscopy and dc polarization measurements. Three different electrolyte supported half-cells were made: the YSZ/PSFN cell with a dense YSZ, the GDC/PSFN cell with a dense GDC electrolyte and the YSZ/GDC/PSFN cell with a dense YSZ electrolyte and a GDC interlayer between the PSFN cathode and the YSZ.

Their respective electrochemical performance was compared as a function of temperature, in air; the polarization resistance of the GDC/PSFN cell was R_p = 0.71 Ω cm^2, while for the YSZ/GDC/PSFN cell, R_p = 1.95 Ω cm^2 at 700 °C, and for

the YSZ/PSFN cell R_p significantly increases (165 Ω cm^2 at 700 °C). From our point of view and from the XRD results, this increase can mainly be assigned to interface reactivity between electrode and electrolyte and to the formation of non-conductive or less-conductive phases, like $SrZrO_3$ and $Pr_2Zr_2O_7$.

To evaluate the GDC interlayer influence on PSFN cathode activity, the overpotential of the YSZ/GDC/PSFN cell was measured at 700 °C under a direct current and during an ageing test of 1000 hours.

The EIS measurements allowed calculating, from the fitting with given equivalents circuits, the parameters at high frequencies, assigned to the O^{2-} transport through the electrode/electrolyte interface, and those at low frequencies, relevant to understand the oxygen reduction mechanisms at the electrode surface and bulk. The PSFN8273 cathode showed a high stability, with a decrease of R_p of about 6% in the first 200 hours and a stable performance up to 1000 hours, making it a suitable candidate as cathode material in solid oxide fuel cells. Surely, the influence of GDC interlayer remains an open issue, and a higher density of the interlayer could lead to the same, higher performance obtained with GDC dense electrolyte in the GDC/PSFN cell and could avoid the formation of the PZO insulating phase.

References

1. V.A.C. Haanappel, J. Mertens, D. Rutenbeck, C. Tropartz, W. Herzhof, D. Sebold, et al. Optimisation of processing and microstructural parameters of LSM cathodes to improve the electrochemical performance of anode-supported SOFCs J. Power Sources, 141 (2005), pp. 216–226 http://dx.doi.org/10.1016/j.jpowsour.2004.09.016
2. A. Barbucci, M. Carpanese, A.P. Reverberi, G. Cerisola, M. Blanes, P.L. Cabot, *et al.* Influence of electrode thickness on the performance of composite electrodes for SOFC. J. Appl. Electrochem., 38 (2008), pp. 939–945. http://dx.doi.org/10.1007/s10800-008-9500-z
3. J. Nielsen, J. Hjelm. Impedance of SOFC electrodes: A review and a comprehensive case study on the impedance of LSM:YSZ cathodes. Electrochim. Acta, 115 (2014), pp. 31–45. http://dx.doi.org/10.1016/j.electacta.2013.10.053
4. C. Nicolella, A. Bertei, M. Viviani, A. Barbucci. Morphology and electrochemical activity of SOFC composite cathodes: II. Mathematical modelling. J. Appl. Electrochem. (2009), pp. 503–511. http://dx.doi.org/10.1007/s10800-008-9691-3
5. A. Mai, V.A.C. Haanappel, S. Uhlenbruck, F. Tietz. Ferrite-based perovskites as cathode materials for anode-supported solid oxide fuel cells Part I. Variation of composition. Solid State Ionics, 176 (2008), pp. 1–14. http://dx.doi.org/10.1016/j.ssi.2005.03.009
6. N.Q. Minh, T. Takahashi. Science and Technology of Ceramic Fuel Cells. Elsevier, Amsterdam (1995)
7. M. Mogensen, N.M. Sammes, G.A. Tompsett. Physical, chemical and electrochemical properties of pure and doped ceria. Solid State Ionics, 129 (2000), pp. 63–94. http://dx.doi.org/10.1016/S0167-2738(99)00318-5
8. K.C. Wincewicz, J.S. Cooper. Taxonomies of SOFC material and manufacturing alternatives. J. Power Sources, 140 (2005), pp. 280–296. http://dx.doi.org/10.1016/j.jpowsour.2004.08.032
9. H.Y. Tu, Y. Takeda, N. Imanishi, O. Yamamoto. $Ln_{0.4}Sr_{0.6}Co_{0.8}Fe_{0.2}O_{3-\delta}$ (Ln = La, Pr, Nd, Sm, Gd) for the electrode in solid oxide fuel cells. Solid State Ionics Solid State Ionics, 117 (1999), pp. 277–281. http://dx.doi.org/10.1016/S0167-2738(98)00428-7
10. R. Hui, C. Sun, S. Yick, C. Decès-Petit, X. Zhang, R. Maric, *et al.* $Ba_{1-x}Pr_xCo_{1-y}FeyO_{3-\delta}$ as cathode materials for low temperature solid oxide fuel cells. Electrochim. Acta., 55 (2010), pp. 4772–4775. http://dx.doi.org/10.1016/j.electacta.2010.03.053
11. D. Ding, X. Li, S.Y. Lai, K. Gerdes, M. Liu. Enhancing SOFC cathode performance by surface modification through infiltration. Energy Environ Sci., 7 (2014), p. 552. http://dx.doi.org/10.1039/c3ee42926a
12. R. Chiba, F. Yoshimura, Y. Sakurai. Properties of $La_{1-y}Sr_yNi_{1-x}Fe_xO_3$ as a cathode material for a low-temperature operating SOFC. Solid State Ionics., 152-153 (2002), pp. 575–582. http://dx.doi.org/10.1016/S0167-2738(02)00374-0
13. S.B.C. Duval, T. Graule, P. Holtappels, J.P. Ouweltjes, G. Rietveld. Evaluation of the Perovskite $(La_{0.8}Sr_{0.2})_{0.95}Fe_{0.8}Ni_{0.2}O_{3-\delta}$ as SOFC Cathode. Fuel Cells., 9 (2009), pp. 911–914. http://dx.doi.org/10.1002/fuce.200900154
14. S. Hashimoto, K. Kammer, P.H. Larsen, F.W. Poulsen, M. Mogensen. A study of $Pr_{0.7}Sr_{0.3}Fe_{1-x}Ni_xO_{3-}\delta$ as a cathode material for SOFCs with intermediate operating temperature. Solid State Ionics, 176 (2005), pp. 1013–1020. http://dx.doi.org/10.1016/j.ssi.2004.09.010

15. R. Pinedo, I.R. De Larramendi, I.G. De Muro, M. Insausti, J.I.R. De Larramendi, M.I. Arriortua, *et al.* Influence of colloidal templates on the impedance spectroscopic behaviour of $Pr_{0.7}Sr_{0.3}Fe_{0.8}Ni_{0.2}O_3$ for solid oxide fuel cell applications. Solid State Ionics., 192 (2011), pp. 235–240. http://dx.doi.org/10.1016/j.ssi.2010.05.057
16. C. Sun, R. Hui, J. Roller. Cathode materials for solid oxide fuel cells: A review. J. Solid State Electrochem., 14 (2010), pp. 1125–1144. http://dx.doi.org/10.1007/s10008-009-0932-0
17. H. Wang, K.J. Yakal-Kremski, T. Yeh, G.M. Rupp, A. Limbeck, J. Fleig, *et al.* Mechanisms of Performance Degradation of (La, Sr)(Co, Fe)$O_{3-\delta}$ Solid Oxide Fuel Cell Cathodes. J. Electrochem. Soc., 163 (2016), pp. F581–F585. http://dx.doi.org/10.1149/2.0031607jes
18. H.J. Choi, Y.H. Na, D.W. Seo, S.K. Woo, S.D. Kim. Densification of gadolinia-doped ceria diffusion barriers for SOECs and IT-SOFCs by a sol-gel process. Ceram. Int., 42 (2015), pp. 545–550. http://dx.doi.org/10.1016/j.ceramint.2015.08.143
19. A. Tsoga, A. Naoumidis, A. Gupta, D. Stöver. Microstructure and Interdiffusion Phenomena in YSZ-CGO Composite Electrolyte. Mater. Sci. Forum., 308–311 (1999), pp. 794–799. http://dx.doi.org/10.4028/www.scientific.net/MSF.308-311.794
20. S. Jung-Hoon, M.G. Jung, H.W. Park, H.-T. Lim. The Effect of Fabrication Conditions for GDC Buffer Layer on Electrochemical Performance of Solid Oxide Fuel Cells. Nano-Micro Lett., 5 (2013), pp. 151–158. http://dx.doi.org/10.5101/nml.v5i3.151-158
21. A. Flura, C. Nicollet, V. Vibhu, J.C. Grenier. Application of the Adler-Lane-Steele Model to Porous $La_2NiO_{4+\delta}$ SOFC Cathode: Influence of Interfaces with Gadolinia Doped Ceria. J. Electrochem. Soc., 163 (2016), pp. 523–532.
22. M.Z. Khan, M.T. Mehran, R.-H. Song, J.-W. Lee, S.-B. Lee, T.-H. Lim, *et al.* Effect of GDC interlayer thickness on durability of solid oxide fuel cell cathode. Ceram. Int., 1–7 (2016). http://dx.doi.org/10.1016/j.ceramint.2016.01.085
23. J. Szasz, F. Wankmuller, V. Wilde, H. Stormer, D. Gerthsen, N.H. Menzler, *et al.* Nature and Functionality of Oxygen/Cathode/Electrolyte-Interfaces in SOFCs. ECS Trans., 66 (2015), pp. 79–87. http://dx.doi.org/10.1149/06602.0079ecst
24. F. Wang, M. Nishi, M.E. Brito, H. Kishimoto, K. Yamaji, H. Yokokawa, *et al.* Sr and Zr Diffusion in LSCF/10GDC/8YSZ Triplets for Solid Oxide Fuel Cells (SOFCs). J. Power Sources., 258 (2014), pp. 281–289. http://dx.doi.org/10.1016/j.jpowsour.2014.02.046
25. L.A. Chick, L.R. Pederson, G.D. Maupin, J.L. Bates, L.E. Thomas, G.J. Exarhos. Glycine-nitrate combustion synthesis of oxide ceramic powders. Mater. Lett., 10 (1990), pp. 6–12. http://dx.doi.org/10.1016/0167-577X(90)90003-5
26. M. Cimenti, V.I. Birss, J.M. Hill. Distortions in Electrochemical Impedance Spectroscopy Measurements Using 3-Electrode Methods in SOFC. II. Effect of Electrode Activity and Relaxation Times. Fuel Cells., 7 (2007), pp. 377–391. http://dx.doi.org/10.1002/fuce.200700020
27. M. Cimenti, A.C. Co, V.I. Birss, J.M. Hill. Distortions in Electrochemical Impedance Spectroscopy Measurements Using 3-Electrode Methods in SOFC. I −Effect of Cell Geometry. Fuel Cells (2007), pp. 364–376. http://dx.doi.org/10.1002/fuce.200700019
28. J.L. Sun, J.X. Wang, C.R. He, P. Shen, Q. Wang, H. Miao, *et al.* Synthesis and electrical properties of screen-printed doped ceria interlayer for IT-SOFC applications. Elsevier B. V. (2015). http://dx.doi.org/10.1016/j.jallcom.2014.12.169
29. F. Mauvy, C. Lalanne, J.-M. Bassat, J.-C. Grenier, H. Zhao, L. Huo, *et al.* Electrode properties of $Ln_2NiO_{4+\delta}$ (Ln = La, Nd, Pr): AC impedance and DC polarization studies. J. Electrochem. Soc., 153 (2006), pp. A1547–A1553. http://dx.doi.org/10.1149/1.2207059
30. B. Hirschorn, M.E. Orazem, B. Tribollet, V. Vivier, I. Frateur, M. Musiani. Determination of effective capacitance and film thickness from constant-phase-element parameters. Electrochim. Acta., 55 (2010), pp. 6218–6227. http://dx.doi.org/10.1016/j.electacta.2009.10.065
31. J. Jamnik, J. Maier. Generalised equivalent circuits for mass and charge transport: chemical capacitance and its implications. Phys. Chem. Chem. Phys., 3 (2001), pp. 1668–1678. http://pubs.rsc.org/en/content/articlehtml/2001/cp/b100180i
32. J. Fleig, A. Schmid, G.M. Rupp, C. Slouka, E. Navickas, L. Andrejs, *et al.* The Chemical Capacitance as a Fingerprint of Defect Chemistry in Mixed Conducting Oxides. Acta Chim Slov., 63 (2016), pp. 1–10. http://dx.doi.org/10.17344/acsi.2016.2302
33. S.B. Adler, J.A. Lane, B.C.H. Steele. Electrode Kinetics of Porous Mixed-Conducting Oxygen Electrodes. J. Electrochem. Soc., 143 (1996), p. 3554. http://dx.doi.org/10.1149/1.1837252
34. Y.L. Yang, A.J. Jacobson, C.L. Chen, G.P. Luo, K.D. Ross, C.W. Chu. Oxygen exchange kinetics on a highly oriented $La_{0.5}Sr_{0.5}CoO_{3-\delta}$ thin film prepared by pulsed-laser deposition. Appl. Phys. Lett., 79 (2001), p. 776. http://dx.doi.org/10.1063/1.1390316

35. T. Kawada, J. Suzuki, M. Sase, A. Kaimai, K. Yashiro, Y. Nigara, *et al.* Determination of Oxygen Vacancy Concentration in a Thin Film of $La_{0.6}Sr_{0.4}CoO_{3-\delta}$ by an Electrochemical Method. J. Electrochem. Soc., 149 (2002), p. E252. http://dx.doi.org/10.1149/1.1479728
36. W. Lai, S.M. Haile. Impedance spectroscopy as a tool for chemical and electrochemical analysis: a case study of Ceria. J. Am. Ceram. Soc., 88 (2005), pp. 2979–2997.
37. J. Xiao, Q. Xu, M. Chen, K. Zhao, B.-H. Kim. Improved overall properties in La_{1-x} Ca_x $Fe_{0.8}Cr_{0.2}O_{3-\delta}$ as cathode for intermediate temperature solid oxide fuel cells. Ionics (Kiel), 21 (2015), pp. 2805–2814. http://dx.doi.org/10.1007/s11581-015-1468-1
38. B. Philippeau, F. Mauvy, C. Nicollet, S. Fourcade, J.C. Grenier. Oxygen reduction reaction in $Pr_2NiO_{4+\delta}$/$Ce_{0.9}Gd_{0.1}O_{1.95}$ and $La_{0.6}Sr_{0.4}Co_{0.2}Fe_{0.8}O_{3-\delta}$/$La_{0.8}Sr_{0.2}Ga_{0.8}Mg_{0.2}O_{2.80}$ half cells: an electrochemical study. J. Solid State Electrochem., 19 (2014), pp. 871–882. http://dx.doi.org/10.1007/s10008-014-2686-6
39. J. Piao, K. Sun, N. Zhang, X. Chen, S. Xu, D. Zhou. Preparation and characterization of $Pr_{1-x}Sr_xFeO_3$ cathode material for intermediate temperature solid oxide fuel cells. J. Power Sources, 172 (2007), pp. 633–640. http://dx.doi.org/10.1016/j.jpowsour.2007.05.023
40. J. Liu, A.C. Co, S. Paulson, V.I. Birss. Oxygen reduction at sol-gel derived $La_{0.8}Sr_{0.2}Co_{0.8}Fe_{0.2}O_3$ cathodes. Solid State Ionics, 177 (2006), pp. 377–387. http://dx.doi.org/10.1016/j.mcm.2006.01.023
41. B. Liu, Y. Zhang, L. Zhang. Oxygen reduction mechanism at $Ba_{0.5}Sr_{0.5}Co_{0.8}Fe_{0.2}O_{3-\delta}$ cathode for solid oxide fuel cell. Int. J. Hydrogen Energy, 34 (2009), pp. 1008–1014. http://dx.doi.org/10.1016/j.ijhydene.2008.10.096
42. X. Huang, J. Liu, Z. Lu, W. Liu, L. Pei, T. He, *et al.* Properties of nonstoichiometric $Pr_{0.6-x}Sr_{0.4}MnO_3$ as the cathodes of SOFCs. Solid State Ionics, 130 (2000), pp. 195–201. http://dx.doi.org/10.1016/S0167-2738(00)00643-3
43. D. Mantzavinos, A. Hartley, I.S. Metcalfe, M. Sahibzada. Oxygen stoichiometries in $La_{1-x}Sr_xCo_{1-y}Fe_yO_{3-\delta}$ perovskites at reduced oxygen partial pressures. Solid State Ionics, 134 (2000), pp. 103–109. http://dx.doi.org/10.1016/S0167-2738(00)00718-9
44. D. Chen, S.R. Bishop, H.L. Tuller. Nonstoichiometry in oxide thin films operating under anodic conditions: A chemical capacitance study of the praseodymium-cerium oxide system. Chem. Mater., 26 (2014), pp. 6622–6627. http://dx.doi.org/10.1021/cm503440v
45. E. Lust, I. Kivi, G. Nurk, P. Moller, S. Kallip, V. Grozovski, *et al.* Influence of Cathode Porosity and Potential on Oxyggen Reduction Kinetics at Intermediate Temperature SOFCs Cathoddes. ECS Trans., 7 (2007), pp. 1071–1080. http://dx.doi.org/10.1149/1.2729204
46. X.J. Chen, K.a. Khor, S.H. Chan. Electrochemical behavior of La(Sr)MnO3 electrode under cathodic and anodic polarization. Solid State Ionics, 167 (2004), pp. 379–387. http://dx.doi.org/10.1016/j.ssi.2003.08.049
47. M.J. Jørgensen, P. Holtappels, C.C. Appel. Durability test of SOFC cathodes. J. Appl. Electrochem., 30 (2000), pp. 411–418. http://dx.doi.org/10.1023/A:1003987318963
48. M. Arnold, T.M. Gesing, J. Martynczuk, A. Feldhoff. Correlation of the formation and the decomposition process of the BSCF perovskite at intermediate temperatures. Chem. Mater., 20 (2008), pp. 5851–5858. http://dx.doi.org/10.1021/cm801463h
49. H.J. Hwang, J.-W. Moon, S. Lee, E.a. Lee. Electrochemical performance of LSCF-based composite cathodes for intermediate temperature SOFCs. J. Power Sources, 145 (2005), pp. 243–248. http://dx.doi.org/10.1016/j.jpowsour.2005.02.063
50. L. Agun, H. Abd. Rahman, S. Ahmad, A. Muchtar. Durability and Stability of LSCF Composite Cathode for Intermediate-Low Temperature of Solid Oxide Fuel Cell (IT-LT SOFC): Short Review. Adv. Mater. Res., 893 (2014), pp. 732–737. http://dx.doi.org/10.4028/www.scientific.net/AMR.893.732
51. Y. Gong, C. Sun, Q.A. Huang, J.A. Alonso, M.T. Fernández-Díaz, L. Chen. Dynamic Octahedral Breathing in Oxygen-Deficient $Ba_{0.9}Co_{0.7}Fe_{0.2}Nb_{0.1}O_{3-\delta}$ Perovskite Performing as a Cathode in Intermediate-Temperature SOFC. Inorg. Chem., 55 (2016), pp. 3091–3097. http://dx.doi.org/10.1021/acs.inorgchem.5b03002
52. H. Taguchi, R. Chiba, T. Komatsu, H. Orui, K. Watanabe, K. Hayashi. LNF SOFC cathodes with active layer using Pr_6O_{11} or Pr-doped CeO_2. J. Power Sources, 241 (2013), pp. 768–775. http://dx.doi.org/10.1016/j.jpowsour.2013.04.141

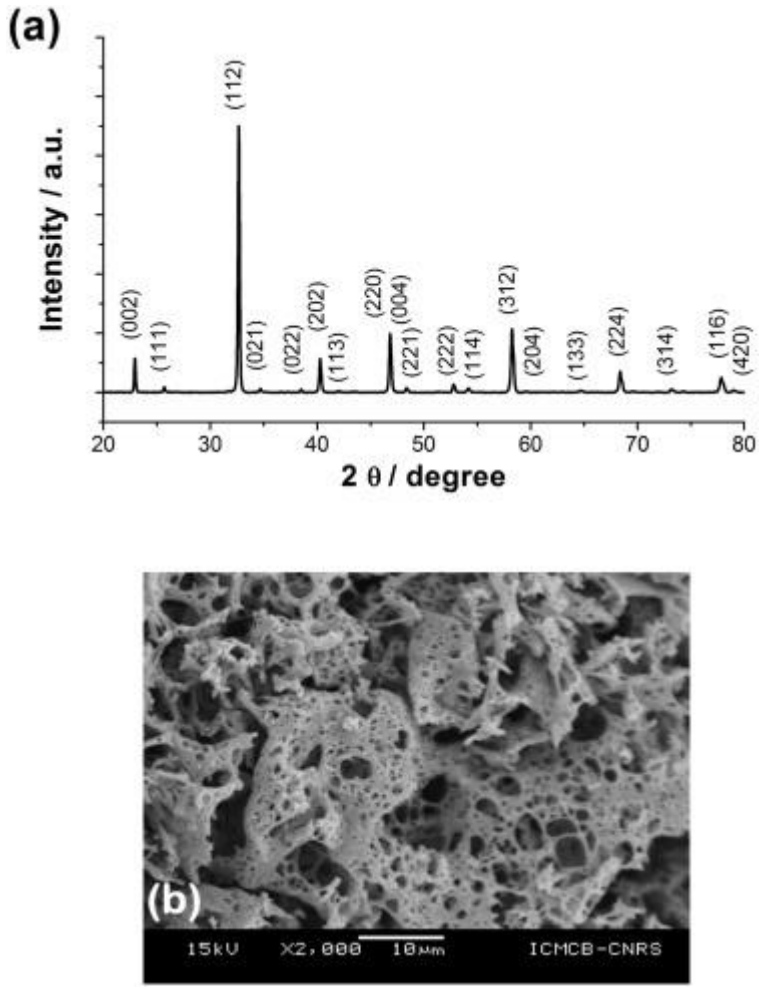

Fig. 1. (a) XRD diagram and (b) SEM micrograph of the annealed PSFN8273 powder.

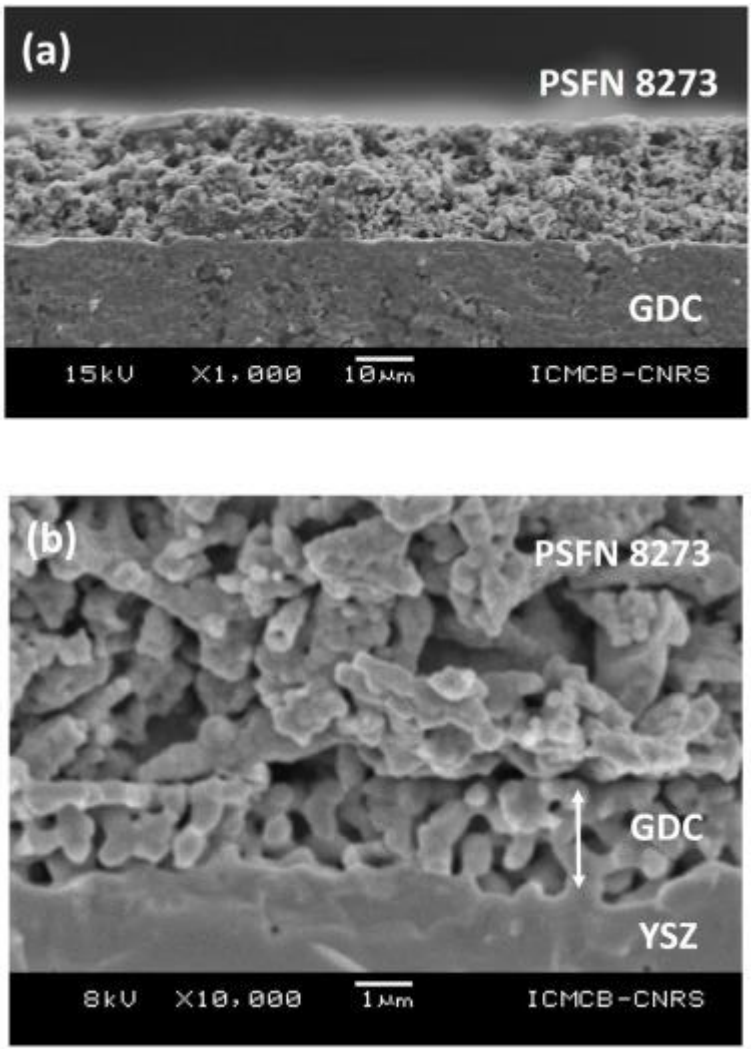

Fig. 2. (a) GDC/PSFN and (b) YSZ/GDC/PSFN cells fractured cross section after the sintering treatment.

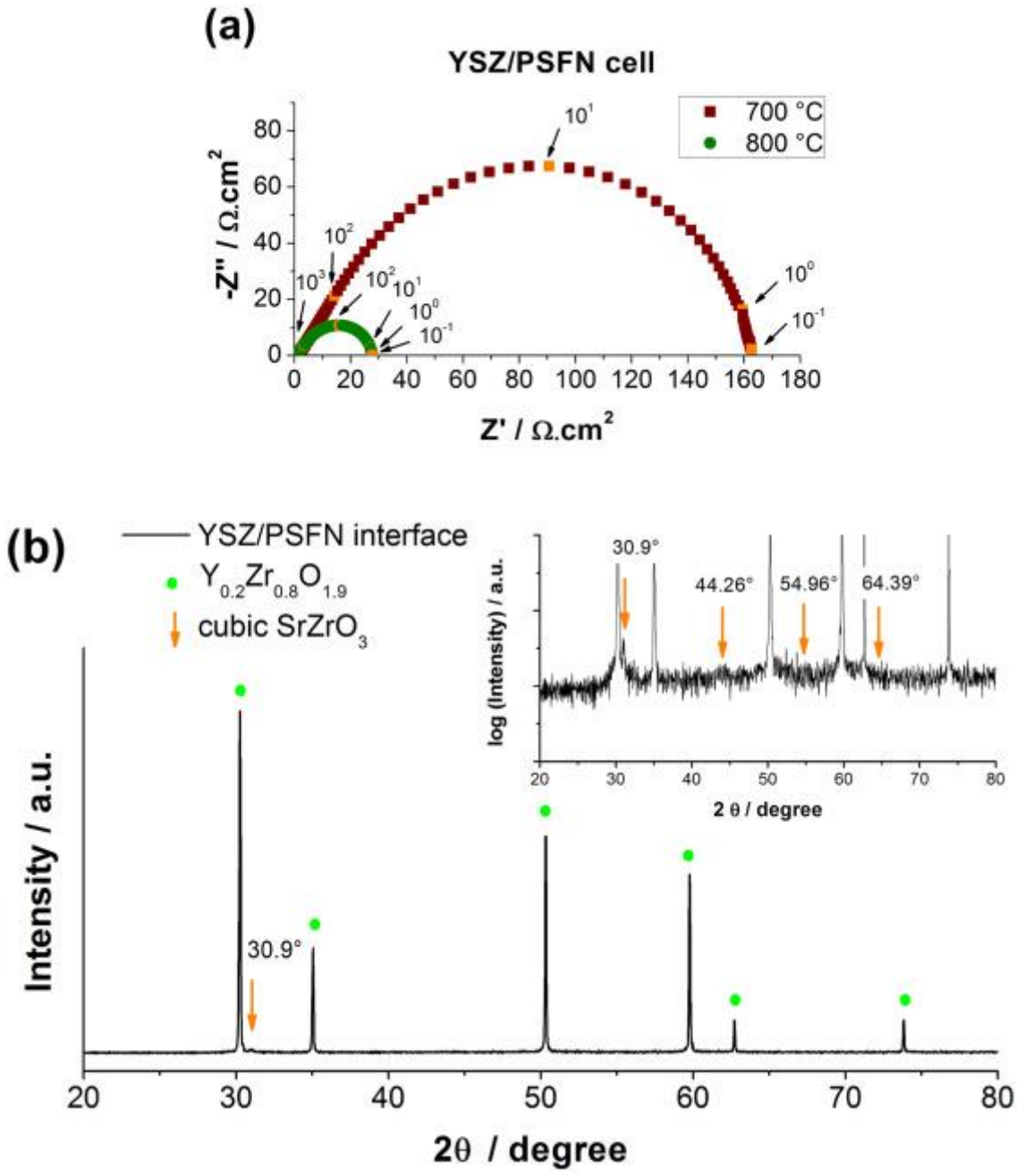

Fig. 3. (a) YSZ/PSFN Nyquist plot at 700 °C and 800 °C and (b) YSZ/PSFN interface XRD pattern after the electrochemical test.

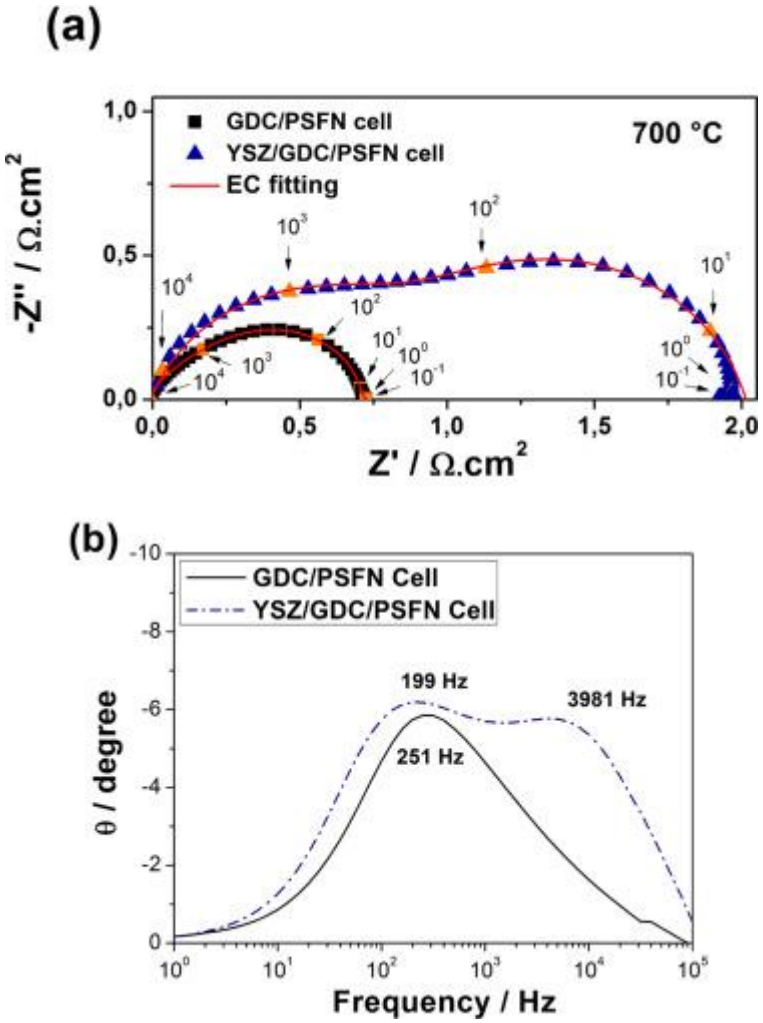

Fig. 4. (a) Nyquist and (b) Bode plots of YSZ/GDC/PSFN cell and GDC/PSFN cell measured under air at 700 °C and i_{dc} = 0.

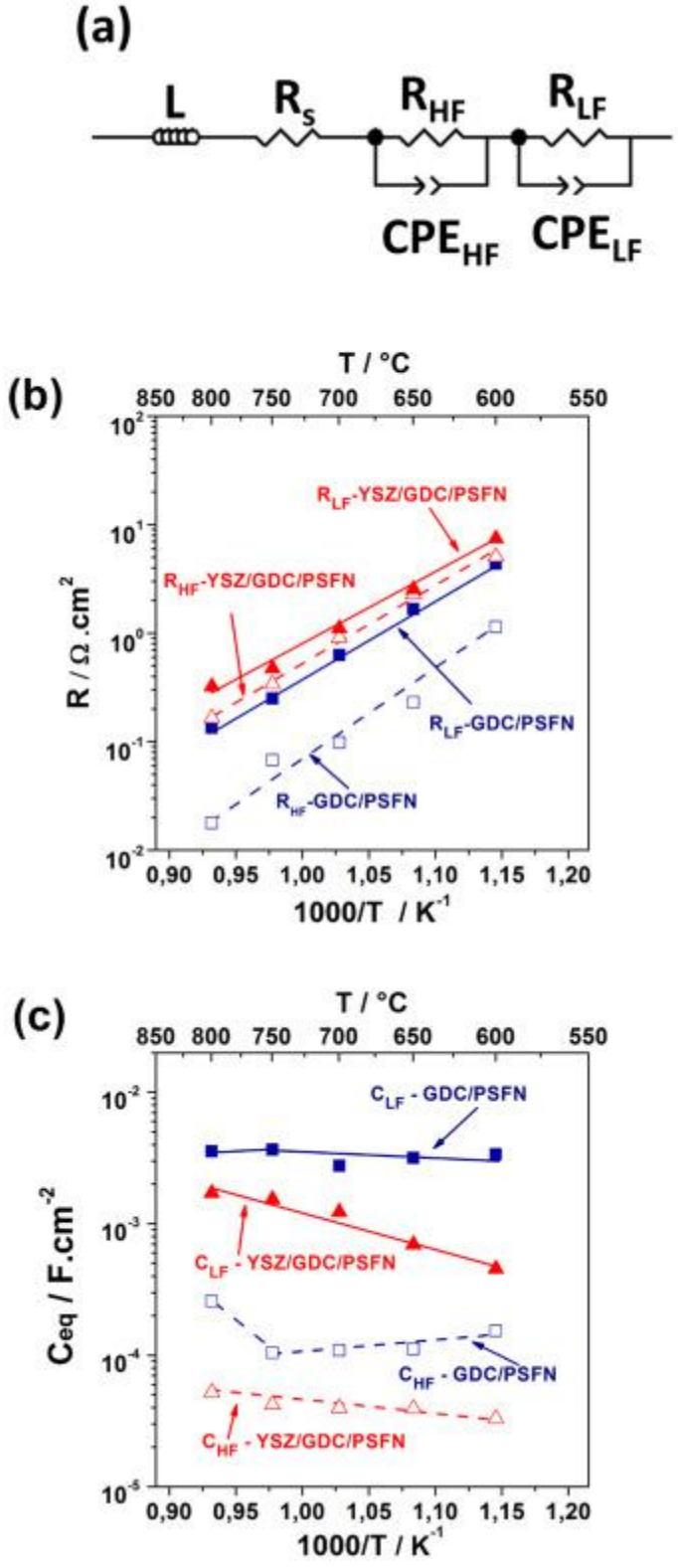

Fig. 5. (a) Equivalent circuit used for the data fitting; (b) Thermal variation of the polarization resistances (R_{HF} and R_{LF}) and (c) of the equivalent capacitances (C_{HF} and C_{LF}).

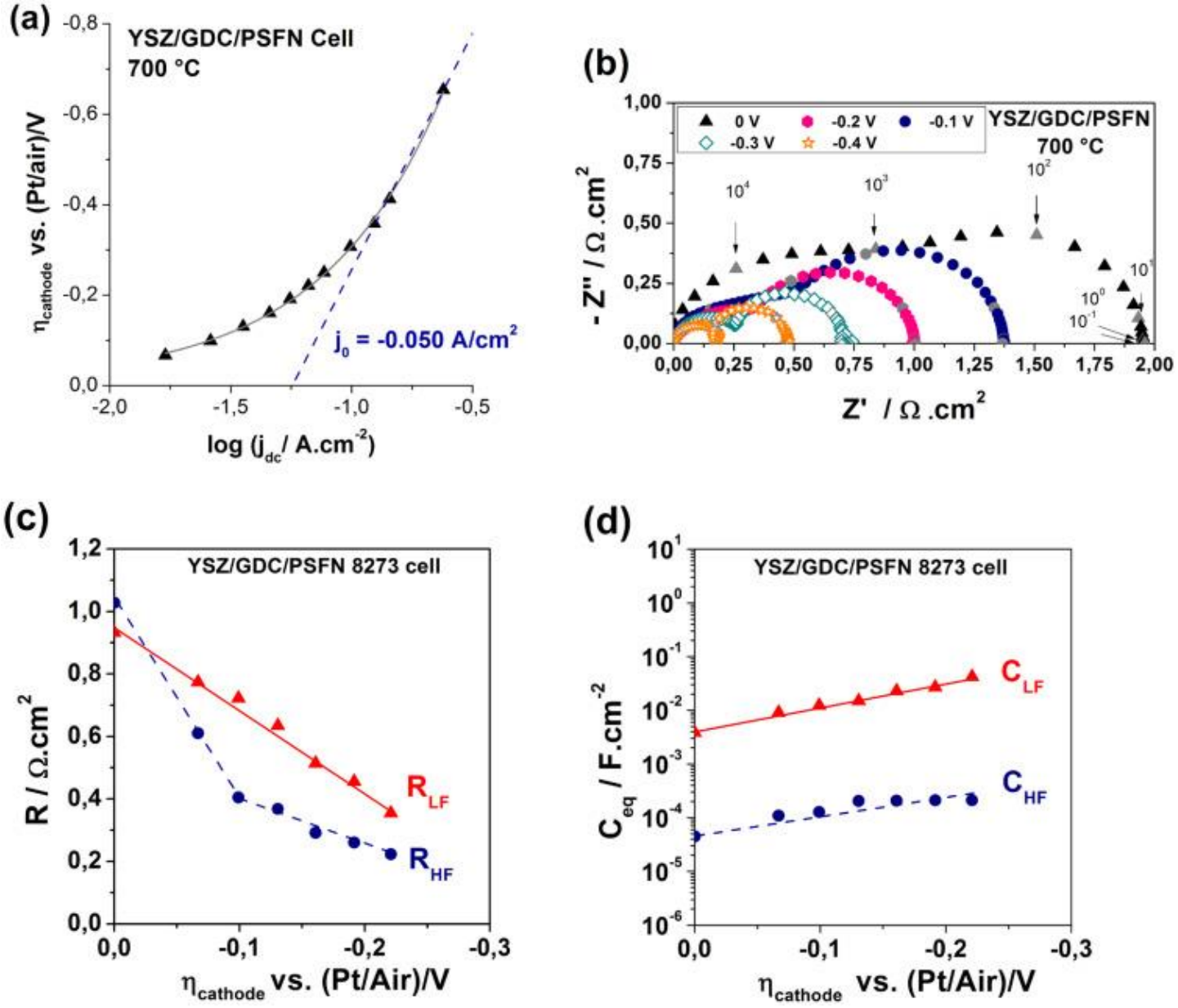

Fig. 6. (a) Cathodic polarization curve for PSFN8273 measured at 700 °C and applied dc bias potential in the range 0 to − 1 V; (b) Nyquist plots of GDC/YSZ/PSFN cell for various bias potentials. Variation of (c) R_{HF} and R_{LF} and (d) C_{HF} and C_{LF} as function of cathodic overpotential ($\eta_{cathode}$) at 700 °C.

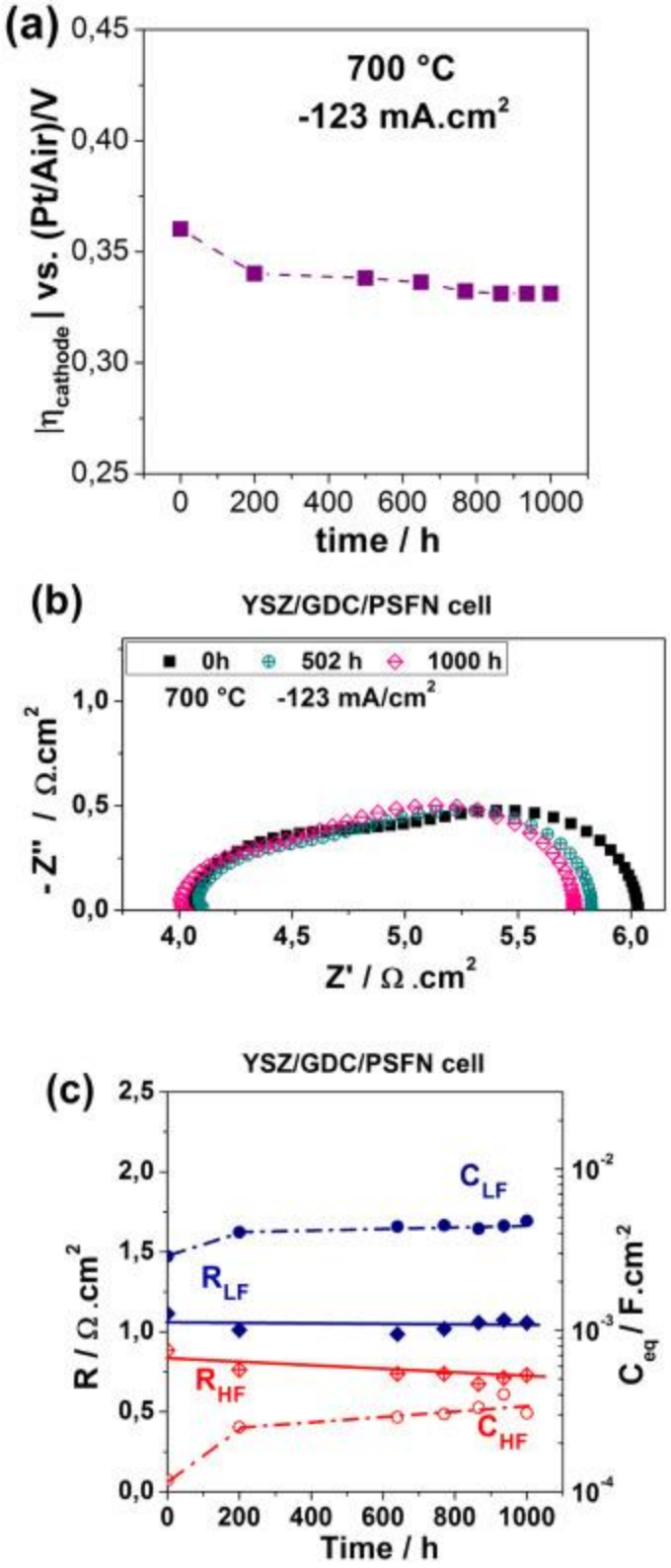

Fig. 7. (a) Time dependence of $|\eta_{cathode}|$, (b) Corresponding impedance diagrams, (c) Time dependence of the polarization resistances R_{HF} and R_{LF} and equivalent capacitances (C_{HF} and C_{LF}), measured at 700 °C under an applied current load of −123 mA.cm^{-2}, periodically interrupted to perform OCV measurements.

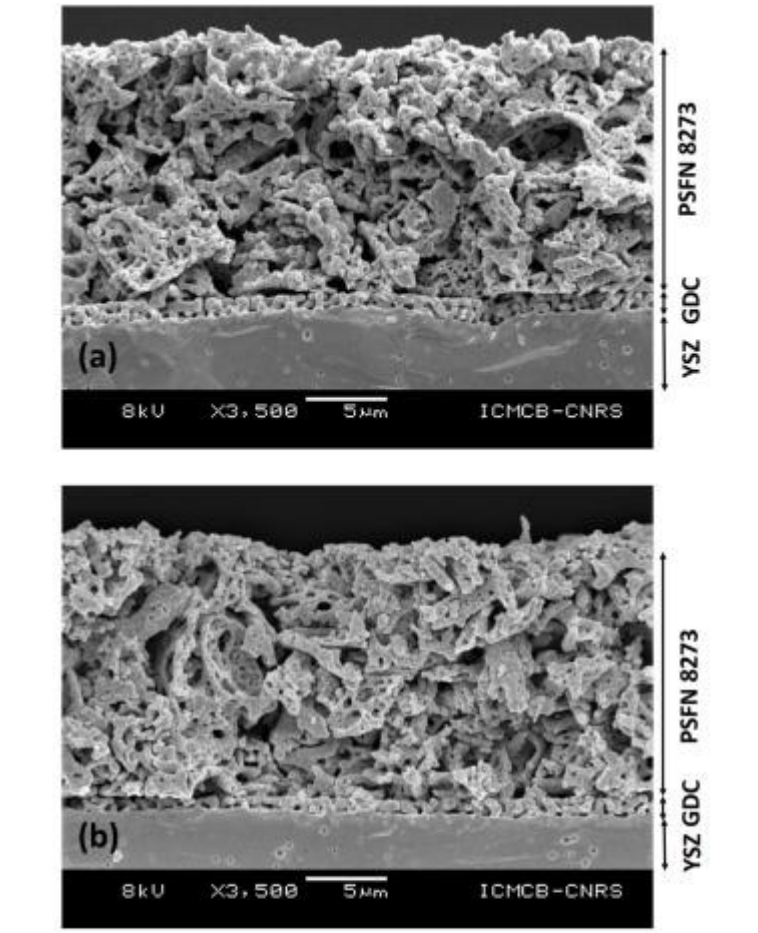

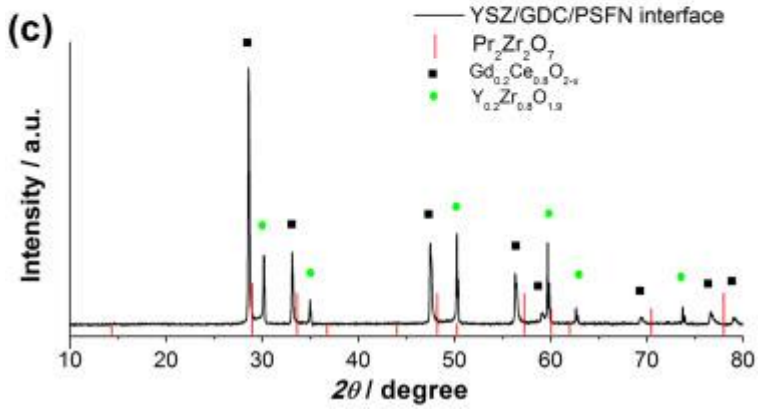

Fig. 8. (a) YSZ/GDC/PSFN cells fractured cross section after the sintering treatment and (b) after the ageing test for 1000 hours; (c) YSZ/GDC/PSFN interface XRD pattern after the sintering treatment.

Table 1
PSFN 8273 R_p values obtained at 700 °C and 800 °C, compared with the literature results for similar compositions.

PSFN 8273 (on GDC)	0.73	0.14	Our results
PSFN 8273 (on GDC/YSZ)	1.95	0.42	Our results
PSFN 7382 (colloidal templates)	3.32	1.22	[15]
PSFN 7373 (point electrode)	2.72	0.22	[14]